Blue Light Excitable Near-Infrared Luminescence Material $Yb_{2-2x}Cr_{2x}W_3O_{12}$: $Cr^{3+}\rightarrow Yb^{3+}$ Energy Transfer, Mechanisms of Antithermal Quenching, and High-Performance pc-LED Applications

Sihan Yang,[a$] Changshuai Gong,[a$] Ziying Wang,[a] Liang Dong,[c] Xuejiao Wang,[a*] Ji-Guang Li[b*]

[a]School of Materials and Environmental Engineering, Bohai University, Jinzhou, Liaoning 121007, China
[b]Research Center for Electronic and Optical Materials, National Institute for Materials Science, Tsukuba, Ibaraki 305-0044, Japan
[c]Key Laboratory for Anisotropy and Texture of Materials (Ministry of Education), School of Materials Science and Engineering, Northeastern University, Shenyang, Liaoning 110819, China

*Corresponding author

Dr. Xuejiao Wang
Bohai University
Jinzhou, China
Tel: +86-416-3400708
Email: wangxuejiao@bhu.edu.cn

Dr. Ji-Guang Li
National Institute for Materials Science
Tsukuba, Japan
Tel: +81-29-860-4394
Email: li.jiguang@nims.go.jp

[$]Sihan Yang and Changshuai Gong made equal contributions to this work

ABSTRACT

To overcome the problem of severe thermal quenching of near-infrared (NIR) phosphors, the NIR phosphor with anti-thermal quenching performance is urgently needed. In this work, negative thermal expansion (NTE) material $Yb_{2-2x}Cr_{2x}W_3O_{12}$ was prepared. Through a comprehensive analysis involving *in-situ* XRD, thermogravimetry (TG) and Rietveld refinement, it was concluded that, at room temperature, the sample adopts a trihydrate orthorhombic structure ($Yb_2W_3O_{12}\cdot 3H_2O$) and does not exhibit negative thermal expansion (NTE) behavior. However, after dehydration at 373 K, anhydrous orthorhombic $Yb_2W_3O_{12}$ (space group *Pbcn*), which exhibits obvious NTE properties, was obtained. The underlying mechanism is that, when water molecules enter the crystal and occupy vacancies, the Yb-O-W bonds bend, restricting the transverse thermal vibrations of the Yb-O-W bonds. The characteristic emission of Yb^{3+} within the range of 800-1300 nm was observed under 468 nm blue light irradiation due to the efficient energy transfer from $Cr^{3+}\rightarrow Yb^{3+}$. Remarkably, the prepared NIR phosphor has anti-thermal quenching performance, and at 398 K the intensity of the strongest emission can maintain 1.89 times that of the room temperature, surpassing most NIR phosphors. The anti-thermal quenching phenomenon is attributed to cell contraction, which reduces the distance between the sensitizer and activator, thereby enhancing the energy transfer efficiency and increasing the luminous intensity. The combination of 460 nm excitable strong NIR emission and anti-thermal quenching suggests potential application in biomedical imaging and infrared night-vision technologies. The NIR pc-LED device, prepared by coating the $Yb_{1.94}Cr_{0.06}W_3O_{12}$ phosphor on a commercial 460 nm chip, demonstrated a high optoelectronic efficiency and high output power, making it well-suited for night vision applications. Furthermore, the efficient NIR-I/II emission from $Yb_{1.94}Cr_{0.06}W_3O_{12}$ was proved to be highly effective for compositional analysis. This study offers valuable insights for designing NIR phosphors with excellent thermal quenching resistance.

KEYWORDS: *blue light excitable phosphor; near-infrared luminescence; anti-thermal quenching; efficient energy transfer; negative thermal expansion*

1. INTRODUCTION

NIR spectroscopy has many benefits, such as rapid detection, non-invasive inspection, and contactless measurements.[1-5] Practical applications of the traditional NIR light sources, however, are restricted due to the low efficiency, large size, and high energy consumption. Intelligence and miniaturization of integrated spectrometers are still facing challenges. Another NIR light source currently being developed is the NIR pc-LED. Compared with conventional light sources, it has a small size, low cost, stable spectrum, and a tunable spectral distribution.[6] Additionally, the NIR pc-LED is suitable as a light source for micro NIR spectrometers owing to the inherent benefits of white LEDs.[7]

Active ions that can realize broadband NIR luminescence can primarily be categorized as 4*f*-5*d* electron transition type (Ce^{3+}, Eu^{2+}, etc.), 6*s*-6*p* electron transition type (Bi^{3+}/Bi^{2+}/Bi^{+}, etc.), and 3*d*-3*d* electron transition type (Cr^{3+}/Cr^{4+}, Ni^{2+}, Fe^{3+}, etc.). Cr^{3+} has garnered significant academic attention due to its ultra-wide emission band, capacity for tunable broadband NIR emission within the 700-1200 nm range, and efficient excitation by blue LED chips. It is thus widely regarded as the most promising activator for the development of commercial NIR pc-LEDs.[8,9] However, the emission of Cr^{3+}-activated phosphors primarily located in the NIR-I region (650-900 nm). Emission in the NIR-II region (1000-1700 nm) has the advantages of covering multiple functional group vibration frequencies, deeper tissue penetration, higher sensitivity, and superior spatial resolution,[10,11] although potential eye safety risk exists for NIR emission >1400 nm in practical use.[12] The emission of Yb^{3+}, originating from *f-f* transitions, lies at the end of the NIR-I region and the beginning of the NIR-II region (＜1400 nm), making it suitable for applications like biological imaging and spectral analysis. However, the intrinsic *f-f* absorption of Yb^{3+} is weak and poorly matches with

commercial blue LED chips. When co-doped with Cr^{3+}, effective $Cr^{3+} \rightarrow Yb^{3+}$ energy transfer may occur, enabling the phosphor to be efficiently excited by blue light and emit high-efficiency NIR light.

In addition, NIR phosphors face a critical challenge, that is, thermal quenching (TQ). Especially, NIR phosphors with longer emission wavelengths often exhibit severe thermal quenching due to strong electron-phonon coupling, which promotes non-radiative transitions. Materials exhibiting negative thermal expansion (NTE) or near-zero thermal expansion (NZTE) behavior provides a new solution for this issue. Among these, the $A_2M_3O_{12}$ family stands out due to its excellent chemical flexibility and adjustable thermal expansion coefficient.[13,14] These compounds consist of co-cornered AO_6 octahedra and MO_4 tetrahedra, and the transverse vibration of the A-O-M bridging bonds can induce NTE behavior at the macroscopic scale. Sumithra et al.[15] systematically studied the thermal expansion properties of the $Ln_2W_3O_{12}$ series (Ln: lanthanide elements) and found that their thermal expansion behavior is regulated by the radius of Ln^{3+} and crystal structure. The tungstates of larger Ln^{3+} (Ln = La, Nd, Dy) exhibit a co-edge monoclinic structure (space group *C2/c*) at room temperature, which suppresses the negative thermal expansion effect. In contrast, the tungstates of smaller Ln^{3+} (Ln = Y, Yb, Er) exhibit a trihydrate orthorhombic structure. Upon dehydration at elevated temperatures, these compounds transform into an orthorhombic phase (space group *Pnca*) and exhibit pronounced NTE behavior. Among them, $Yb_2W_3O_{12}$, as a typical negative thermal expansion material, has a linear thermal expansion coefficient of -8.35×10^{-6} K^{-1}@373-873 K, in sharp contrast to traditional positive thermal

expansion materials such as YAG (8.5×10^{-6} K^{-1}@300-600 K) and YAP (8.325×10^{-6} K^{-1}@298-774 K).[15–17] The lattice contraction during heating reduces the distance between activator ions, thereby enhancing energy transfer efficiency and improving luminescence performance.[18,19] Based on this background, this study attempts to incorporate Cr^{3+} into the $Yb_2W_3O_{12}$ matrix, aiming to exploit its negative thermal expansion properties and build an efficient energy transfer pathway from Cr^{3+} to Yb^{3+}. This will facilitate the realization of high-performance NIR-I/II emission and allow to explore the correlation between anomalous thermal quenching behavior and lattice contraction.

In this work, we doped Cr^{3+} into $Yb_2W_3O_{12}$ to study NIR luminescence characteristics and energy transfer mechanism. The mechanism of anti-thermal quenching and multi-functional applications were also explored. The $Yb_{2-2x}Cr_{2x}W_3O_{12}$ series samples were synthesized *via* traditional solid-state reaction method. The NIR emission from the Yb^{3+} ions can be produced under blue light irradiation owing to the energy transfer of $Cr^{3+}\rightarrow Yb^{3+}$. The representative $Yb_{1.94}Cr_{0.06}W_3O_{12}$ sample maintains 189% of its luminescence intensity at 398 K, surpassing the performance of most long-wavelength-emitting NIR phosphors. An NIR pc-LED device was also constructed using a commercial 460 nm blue LED chip and $Yb_{1.94}Cr_{0.06}W_3O_{12}$ phosphor. The results showed that $Yb_{1.94}Cr_{0.06}W_3O_{12}$ phosphor has potential application in high-performance NIR pc-LED.

2. EXPERIMENTAL SECTION

2.1 Sample preparation

The conventional solid-state reaction method was selected over wet-chemical synthesis sol-gel, due to its superior scalability for potential industrial applications. The

rare earth source for the synthesis is Yb_2O_3 (99.99% pure), which was purchased from Huizhou Ruier Rare Chemical Hi-Tech Co. Ltd. (Huizhou, China). The other reagents of $H_{40}N_{10}O_{41}W_{12}{\cdot}xH_2O$ (AR grade) and Cr_2O_3 (99.99% pure) were purchased from Aladdin Corporation (Shanghai, China) and were used without further purification. The starting materials were weighed based on the calculated molar stoichiometric ratios, and then transferred into an agate mortar, where a suitable quantity of alcohol was added to achieve full grinding. The powder mixture was transferred into a corundum crucible after drying, and the crucible was then put inside a tube furnace and heated for 4 h at 1100 ℃. Thereafter, the sample was cooled to room temperature followed by grounding into powder for further experiments.

2.2 Characterization

The phases of the obtained specimens were determined with an Ultima IV X-ray diffractometer (XRD) from Rigaku using a Cu-$K_{\alpha1}$ radiation (λ = 0.15406 nm) in step-scan mode. The inductively coupled plasma-mass spectrometry (ICP-MS; Model ICPE-9820, Shimadzu, Japan) was used to evaluate the Cr^{3+} concentration in the products. The EDS and morphological analyses of the prepared phosphors were conducted utilizing a Tescan MIRA LMS field emission SEM (FE-SEM) system. Diffuse reflectance spectra were acquired using a PE-750 UV-Vis spectroscopy system from PerkinElmer. The Raman and Fourier transform infrared (FT-IR) spectra were acquired utilizing a HORIBA-LabRAM HR confocal micro-Raman spectrometer and an IRTracer-100 spectrometer, respectively. Thermogravimetric curves were measured with an STA 8000 thermal analyzer from PerkinElmer. The PL/PLE and fluorescence decay curves were obtained utilizing an FLS 1000 fluorospectrophotometer from Edinburgh Instru-ments Ltd. Temperature-dependent luminescence spectra were also acquired utilizing the same setup coupled to a TAP-02 high-temperature controller.

2.3 Testing and packaging of pc-LED

The NIR pc-LED devices were fabricated utilizing the synthesized $Yb_{1.94}Cr_{0.06}W_3O_{12}$ phosphor and a 460 nm LED (3 W) from San'an Optoelectronics Co., Ltd. The chip material used is InGaN, while the bracket pin material is copper alloy with a silver-plated surface. Epoxy resin is used as the encapsulating material. The encapsulation process is as follows: First, the phosphor and epoxy resin are mixed in a specific ratio to ensure the materials are fully dispersed. Next, the mixture is degassed using a degassing machine to remove any air bubbles, ensuring high uniformity and stability of the mixture. Finally, the mixture is applied to the LED chip for further testing.

3. RESULTS AND DISCUSSION

3.1 Phase, crystal structure, morphology and composition

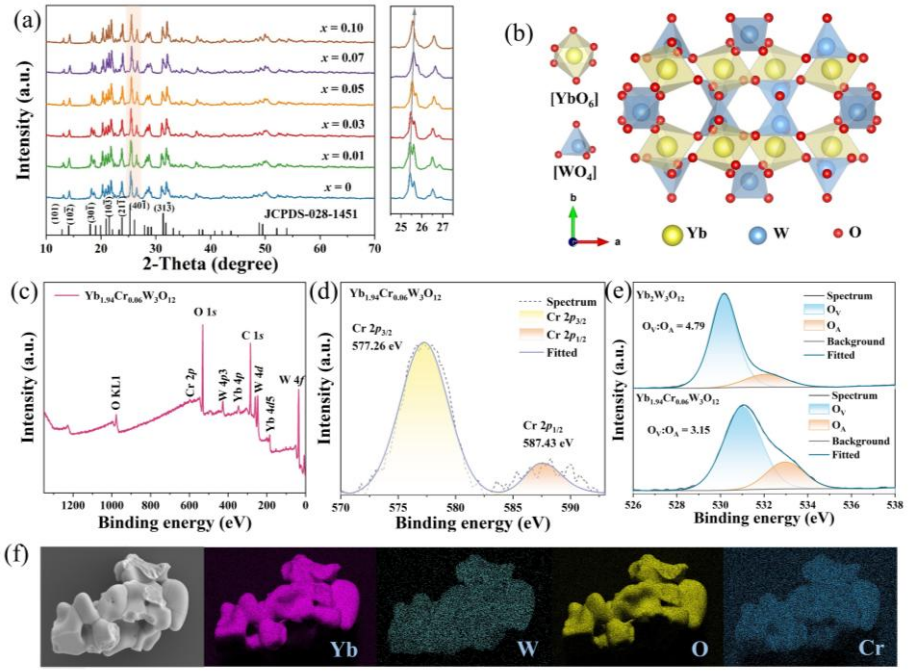


Figure 1. (a) The XRD patterns for the $Yb_{2-2x}Cr_{2x}W_3O_{12}$ (x = 0-0.10) phosphors and enlarged view of the XRD peak in the 2θ = 24.5-27.5° range. (b) The crystal structure of orthorhombic $Yb_2W_3O_{12}$. (c) The survey XPS spectrum of $Yb_{1.94}Cr_{0.06}W_3O_{12}$. (d) High-resolution XPS spectra of Cr 2*p* and (e) O 1*s*. (f) The acquired FE-SEM images and EDS mapping results for the $Yb_{1.94}Cr_{0.06}W_3O_{12}$ phosphor.

A series of $Yb_2W_3O_{12}$ based phosphors doped with different concentrations of Cr^{3+}

were prepared and the actual amounts of Cr^{3+} in the samples were further determined by ICP-MS. The results in Table S1 show that the actual content is quite close to the designed value. The XRD patterns for the series of samples $Yb_{2-2x}Cr_{2x}W_3O_{12}$ (x = 0-0.10) are provided in Figure 1a. All the diffraction peaks of each sample match well with the standard data (JCPDS-18-1451)[20] without detectable impurity signals, indicating the successful synthesis of pure-phase materials and that Cr^{3+} doping did not affect the phase composition. A magnified view of the main diffraction peaks between 24.5°-27.5° reveals a gradual shift toward higher angles with increasing Cr^{3+} concentration. This observation suggests lattice contraction, which can be attributed to the smaller ionic radius of Cr^{3+} (0.615 Å, CN = 6) than Yb^{3+} (0.87 Å CN = 6).[21] The structure of $Yb_2W_3O_{12}$ is presented in Figure 1b, where [YO_6] octahedron and [WO_4] tetrahedron are connected through an oxygen atom. Figure 1c depicts the XPS survey spectrum for the $Yb_{1.94}Cr_{0.06}W_3O_{12}$ sample. It is evident that all the constituent elements of the tested sample can be clearly identified. The high-resolution XPS spectrum of the Cr 2*p* orbital is presented in Figure 1d. The sub-peaks corresponding to Cr $2p_{1/2}$ and Cr $2p_{3/2}$ exhibit central energies of approximately 587.43 eV and 577.26 eV, indicating a trivalent state of Cr.[22] In previously reported studies on $Yb_2W_3O_{12}$, the presence of oxygen vacancies has been documented, making it necessary to use XPS to verify the changes in vacancy concentrations in the samples. Figure 1e displays the O 1*s* spectra of two representative samples, where the fitted high-energy and low-energy peaks are assigned to adsorbed oxygen (O_A) and oxygen vacancies (O_V), respectively.[23] The content of oxygen vacancies can be roughly estimated by the O_V/O_A peak area ratio. Upon Cr^{3+} doping, this ratio decreased from 4.79 to 3.15, indicating a reduction in oxygen vacancy concentration. This reduction would decrease the non-radiative

recombination centers, thereby enhancing luminescence efficiency. Additionally, electron paramagnetic resonance (EPR) spectroscopy was conducted, as displayed in Figure S1. Compared with pristine $Yb_2W_3O_{12}$, the EPR signal of oxygen vacancies (g = 2.003) in $Yb_{1.94}Cr_{0.06}W_3O_{12}$ is significantly reduced, further supporting the conclusion that Cr^{3+} doping leads to a decrease in oxygen vacancy concentration. The SEM and EDS mapping results obtained for the $Yb_{1.94}Cr_{0.06}W_3O_{12}$ phosphor are summarized in Figure S2 and Figure 1f. It was found that the microscopic morphology under different magnifications was not uniform, and the product is agglomerated particles. The mapping results confirmed that all the elements, especially the doped Cr element, were distributed evenly within the prepared sample.[24]

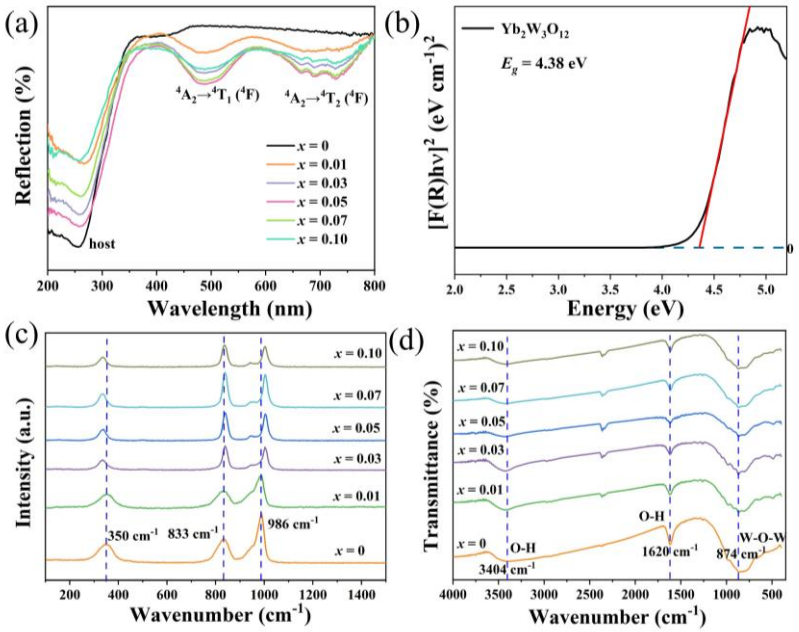


Figure 2. (a) DR spectra of $Yb_{2-2x}Cr_{2x}W_3O_{12}$ (x = 0-0.10). (b) Band gap determination of $Yb_2W_3O_{12}$. (c) Raman spectra, (d) FT-IR spectra obtained for the $Yb_{2-2x}Cr_{2x}W_3O_{12}$ (x = 0-0.10) phosphors.

The DR spectra acquired for the $Yb_{2-2x}Cr_{2x}W_3O_{12}$ (x = 0-0.10) phosphors are presented in Figure 2a, where the $Yb_2W_3O_{12}$ matrix exhibits an absorption band in the 200–350 nm region. Upon Cr^{3+} doping, new absorption bands appeared at 400–550 and

600–800 nm, corresponding to the transitions of Cr^{3+} from the ground state $^4A_2$ to $^4T_1$ (^4F) and $^4T_2$ (^4F), respectively. The band gap energy for $Yb_2W_3O_{12}$ was determined by the Kubelka-Munk function:[25]

$$[F(R_\infty)h\nu]^{1/n} = A(h\nu - E_g) \quad (1)$$

$$F(R_\infty) = (1 - R_\infty)^2/2(R_\infty) \quad (2)$$

Here, $F(R_\infty)$ denotes the reflection coefficient, E_g corresponds to the band gap, A represents a constant, $h\nu$ denotes the energy of the incident photons, whereas n denotes the band gap type, with n = 1/2 for a direct allowed transition, n = 3/2 for a direct forbidden transition, n = 2 for an indirect allowed transition, and n = 3 for an indirect forbidden transition.[26] According to previous reports, the electronic band structure of $Yb_2W_3O_{12}$ is an indirect allowed transition, so the n value is 2. The correlation between $h\nu$ and $[F(R_\infty)h\nu]^{1/2}$ for $Yb_2W_3O_{12}$ is shown in Figure 2b, and the resulting E_g value is 4.38 eV. The Raman and FT-IR spectra were acquired to gather lattice vibration information, which was used to evaluate the phonon energy of both the host lattice and the doped samples. The lattice vibration information was obtained by monitoring Raman and FT-IR spectra to obtain the phonon energy of the prepared samples. As depicted in Figure 2c, the three distinct signals, observed at 250-400 cm^{-1}, 750-900 cm^{-1} and 900-1050 cm^{-1} in the Raman curves, can be identified as the bending vibrations, asymmetric stretching vibrations, and symmetric stretching vibrations of $[WO_4]$ tetrahedra, respectively.[27,28] As illustrated in Figure 2d, the FT-IR spectra of both the host lattice and the series of doped samples exhibited an absorption signal at 874 cm^{-1}, corresponding to the vibrations of W-O-W. Additionally, the signals at 1620 and 3404 cm^{-1} were linked to the H-O-H bending vibration and O-H stretching vibrational modes, respectively.[29]

3.2 Near-infrared luminescence characteristics and efficient Cr^{3+}-Yb^{3+} energy transfer

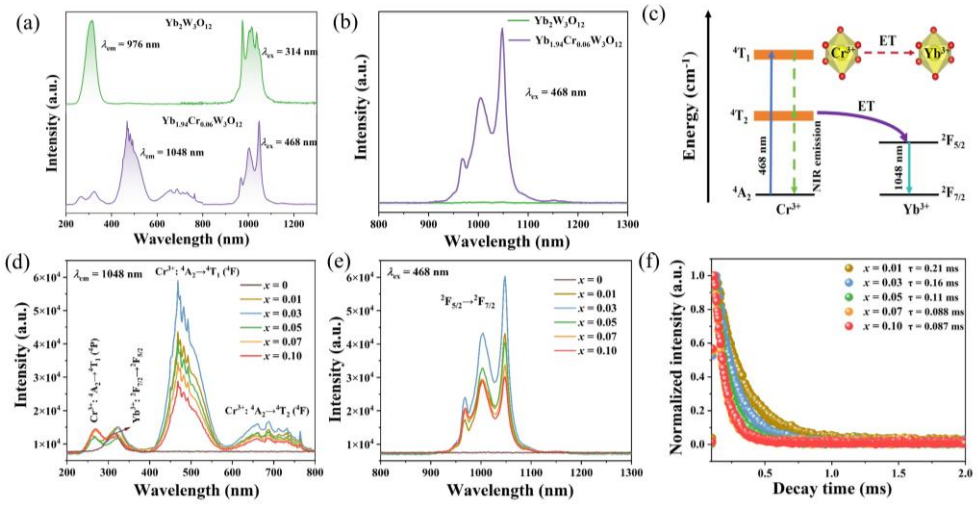


Figure 3. (a) Normalized PL and PLE spectra of $Yb_2W_3O_{12}$ and $Yb_{1.94}Cr_{0.06}W_3O_{12}$. (b) The PL spectra under 468 nm excitation of $Yb_2W_3O_{12}$ and $Yb_{1.94}Cr_{0.06}W_3O_{12}$. (c) The energy transfer schematic diagram between Yb^{3+} and Cr^{3+}. (d) The PLE spectra and (e) PL spectra of $Yb_{2-2x}Cr_{2x}W_3O_{12}$ (x = 0-0.10). (f) Decay curves of the 1048 nm emission of $Yb_{2-2x}Cr_{2x}W_3O_{12}$ (x = 0.01-0.10).

The PL and PLE spectra of the host and Cr^{3+}-doped samples are displayed in Figure 3a and Figure S3. The optimal excitation band of the host sample is located at 314 nm, which does not match commercially available blue LED chips. Under 314 nm excitation, an emission band ranging from 900 to 1100 nm can be observed, attributable to the $^2F_{5/2}\rightarrow{}^2F_{7/2}$ transition of Yb^{3+}. The splitting observed in the emission spectrum can be ascribed to the transitions from the Stark split energy levels of $^2F_{5/2}$ to ground state $^2F_{7/2}$.[30] After doping with Cr^{3+}, no characteristic emission band of Cr^{3+} was detected aside from the Yb^{3+} emission. Furthermore, when monitoring the excitation spectrum at the Yb^{3+} emission wavelength, excitation bands corresponding to the characteristic transitions of Cr^{3+} were observed, indicating an effective energy transfer of $Cr^{3+}\rightarrow Yb^{3+}$. To further verify the existence of energy transfer, as depicted in Figure 3b, the host and Cr^{3+}-doped $Yb_2W_3O_{12}$ samples were excited with blue light under

identical conditions. It can be seen that only the Cr^{3+}-doped sample could be effectively excited by blue light and exhibited Yb^{3+} emission. The absence of Cr^{3+} emission can be attributed to the exceptionally high efficiency of energy transfer from Cr^{3+} to Yb^{3+}. The energy transfer mechanism is illustrated in Figure 3c. Under the blue light irradiation, the electrons within Cr^{3+} transited from the $^4A_2$ ground level to the excited level $^4T_1$, before relaxing down to the excited state $^4T_2$. After that, some of them returned to the ground state $^4A_2$ to produce the NIR light. The other part transferred energy to the Yb^{3+} ions from the $^4T_2$ state of Cr^{3+} to the $^2F_{5/2}$ state of Yb^{3+}. Finally, the electrons at the $^2F_{5/2}$ energy level return to $^2F_{7/2,}$ producing the emission of 1048 nm.[31,32] The excitation spectra obtained for the $Yb_{2-2x}Cr_{2x}W_3O_{12}$ (x = 0-0.10) phosphors are depicted in Figure 3d. The characteristic $^4A_2 \rightarrow {}^4T_1$ (^4P), $^4A_2 \rightarrow {}^4T_2$ (^4F), and $^4A_2 \rightarrow {}^4T_1$ (^4F) transitions of Cr^{3+} were observed as the emission wavelength was being monitored at the 1048 nm emission of Yb^{3+}, exhibiting effective $Cr^{3+} \rightarrow Yb^{3+}$ energy transfer. Under 468 nm excitation, $Yb_2W_3O_{12}$ exhibits no emission peak in the 900-1100 nm region. In contrast, all the $Yb_{2-2x}Cr_{2x}W_3O_{12}$ (x = 0.01-0.10) phosphors displayed the characteristic Yb^{3+} emission at 1048 nm, covering both the NIR-I and NIR-II regions. In summary, it is the highly efficient $Cr^{3+} \rightarrow Yb^{3+}$ energy transfer that enables $Yb_{2-2x}Cr_{2x}W_3O_{12}$ to be effectively excitable by blue light and produce efficient NIR-I/II emission. The emission intensity reached a maximum value at x = 0.03 with an increase in the doping concentration of Cr^{3+} and subsequently decreased (Figure 3e). The full width at half maximum (FWHM) values of the samples were calculated and summarized in Table S2. The decay spectra of the 970 nm, 1004 nm, and 1048 nm emissions of the Yb_{2-}

$_{2x}Cr_{2x}W_3O_{12}$ (x = 0.01-0.10) phosphors were measured., and the results are shown in Figure 3f and Figure S4. Bi-exponential fitting demonstrated the best fitting results and goodness-of-fit factors compared to single and triple exponential fitting (Figure S5). The fitting formula is as follows:[33]

$$I(t) = A_1\exp(-t/\tau_1) + A_2\exp(-t/\tau_2) \qquad (3)$$

where $I(t)$ indicates the emission intensity at time t, τ_1 and τ_2 refer to the lifetimes of the two exponential decaying components, while A_1 and A_2 are constants. The mean lifetime τ^* was determined *via* eq. (4):

$$\tau^* = \frac{A_1{\tau_1}^2 + A_2{\tau_2}^2}{A_1\tau_1 + A_2\tau_2} \qquad (4)$$

The lifetime of the Yb^{3+} ions was calculated by eqs. (3)-(4), with the fitted parameter values and fitting factors χ^2 being summarized in Table S3-5. It was found that as the Cr^{3+} concentration increased, the lifetimes of the three split emission peaks gradually decreased. Additionally, the lifetime values for the three emission peaks at each concentration point showed minimal differences. This suggests that all the three peaks correspond to the $^2F_{5/2} \rightarrow {}^2F_{7/2}$ transition of Yb^{3+}, and thus similar lifetimes and consistent lifetime variations were resulted. Besides, the internal quantum efficiency of $Yb_{1.94}Cr_{0.06}W_3O_{12}$ is 23.6% (Figure S6). Broadband NIR phosphors with emission wavelengths toward NIR-II region have rarely been reported and often have low quantum efficiency, as exemplified by $CaScAlSiO_6$: Cr^{3+} (IQE = 21%, λ_{em} = 950 nm), $InTaO_4$: Cr^{3+} (IQE = 26%, λ_{em} = 975 nm), $Cs_2NaInCl_6$: Cr^{3+} (IQE = 19.7%, λ_{em} = 958 nm), $Cs_2AgInCl_6$: Cr^{3+} (IQE = 5.8%, λ_{em} = 998 nm), and $ZnWO_4$: Cr^{3+} (IQE = 12.5%, λ_{em} = 987 nm).[34–37]

3.3 Anti-thermal quenching NIR luminescence

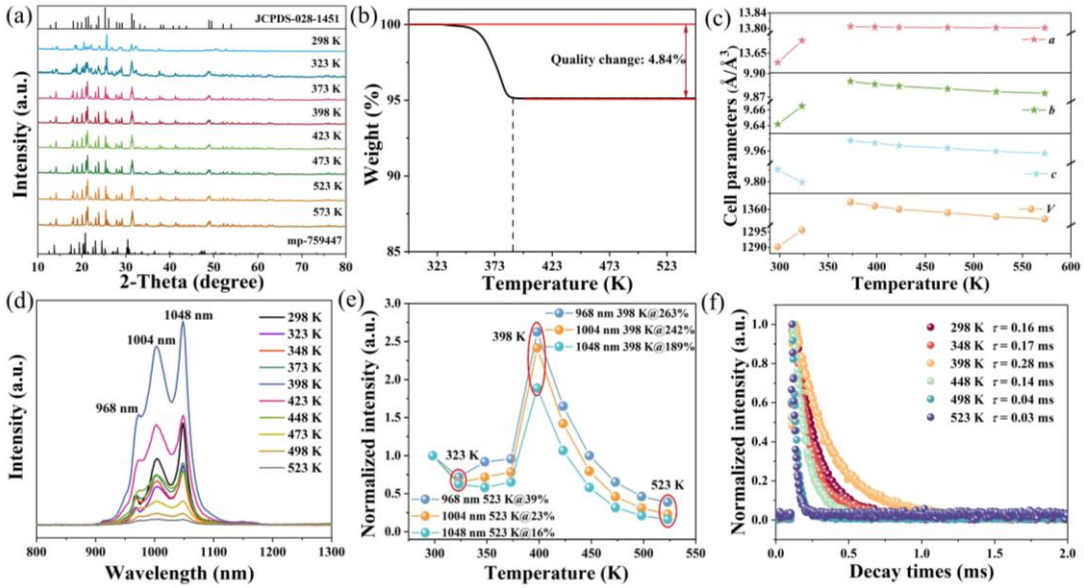


Figure 4. (a) *In-situ* XRD patterns, (b) the TG cures of $Yb_{1.94}Cr_{0.06}W_3O_{12}$. (c) The variation trend of cell parameters *a*, *b*, *c* and *V* with temperature. (d) Temperature-dependent emission spectra, (e) the normalized emission intensity for different emissions of $Yb_{1.94}Cr_{0.06}W_3O_{12}$. (f) Decay curves of the 1048 nm emission for the $Yb_{1.94}Cr_{0.06}W_3O_{12}$ phosphor under varying temperatures.

To evaluate the NTE properties, the *in-situ* XRD patterns of the representative $Yb_{1.94}Cr_{0.06}W_3O_{12}$ sample were taken. As shown in Figure 4a, a phase transition occurred with increasing temperature. When the temperature exceeds 323 K, the XRD patterns can be indexed to the standard reference (mp-759447) of orthorhombic $Yb_2W_3O_{12}$ with *Pbcn* space group. The $A_2M_3O_{12}$ phase is reported to possess microchannels along the *a*-axis. Larger microchannels allow the free entering of water molecules, which disrupt the local structure and lead to partial amorphization of the $Yb_2W_3O_{12}$ phase at room temperature, accompanied by the loss of NTE behavior.[38] At moderately elevated temperatures (~373 K), dehydration occurs and $Yb_2W_3O_{12}$ crystallizes into the orthorhombic system (*Pbcn* space group). This transformation has been observed in all hygroscopic tungstates and orthorhombic tungstates. To verify this phenomenon, we examined the TG curve (Figure 4b), which shows a 4.84% weight loss between 323-388 K by the release of hydration water, indicating a phase transition

during the water release process. The number of water molecules calculated from the TG analysis is approximately equal to 3. For further analysis, Rietveld refinement on the *in-situ* XRD spectra was performed. Since no CIF file is available for hydrated $Yb_2W_3O_{12}\cdot 3H_2O$, we obtained basic crystallographic parameters by unit cell refinement in Jade software using the monoclinic system according to literature reports.[38,39] For the anhydrous sample (orthorhombic system), refinement was conducted using the GSAS software package with the results shown in Figure S7. Detailed crystallographic parameters are listed in Table S6, and the refinement further confirmed the occupation of Yb^{3+} sites by Cr^{3+}. The trend of change in unit cell parameters with temperature is plotted in Figure 4c. It is evident that the hydrated $Yb_2W_3O_{12}\cdot 3H_2O$ sample has smaller unit cell parameters, which is due to the bending of Yb-O-W bonds when water molecules enter the crystal framework and occupy vacancies. After water release, the Yb-O-W bonds become unbent, causing the lattice parameters to increase. Due to the bent Yb-O-W bonds, the hydrated $Yb_2W_3O_{12}\cdot 3H_2O$ may not exhibit negative thermal expansion.[40] When the temperature rises from 298 K to 323 K, the vibrations of the water molecules become more intense. With increasing vibrational activity, the water molecules undergo a transition from a bound sate to a free state, resulting in significant expansion of the unit cell.[41] After complete release of water (373-573 K), cell volume gradually decreases, confirming the presence of NTE characteristics. Additionally, using relevant formulas, the coefficient of thermal expansion in the 373-573 K temperature range was determined to be -2×10^{-5} K^{-1}, further confirming the NTE behavior of the sample. The lattice contraction is caused by the transverse thermal vibrations of the bridging oxygen atoms at the vertices of the Yb-O-W chains, accompanied by slight distortions of the rigid [YbO_6] and [WO_4] polyhedrons.[42]

Generally, the NTE property would lead to thermal enhancement of luminescence.

To investigate this effect, the temperature-dependent luminescence spectra of the sample were taken in Figure 4d. It was found that the emission intensity initially decreased, which is followed by an increasing trend before decreasing again with an increase in temperature. As analyzed above, the hydrated $Yb_2W_3O_{12}\cdot 3H_2O$ sample exhibits no NTE. However, upon dehydration, it clearly demonstrates characteristic NTE behavior. The relationship between emission intensity and temperature can be seen by the normalized spectra of different emissions in Figure 4e. The emission peaks at 970 nm, 1004 nm, and 1048 nm show consistent changes with increasing temperature. At 398 K, the emission intensities increased to 263%, 242%, and 189% of their room temperature values, respectively. These values significantly surpass those of typical NIR-II emitting phosphors, confirming the excellent anti-thermal quenching property of the sample in practical applications. This fluorescence enhancement phenomenon is attributed to the lattice contraction of $Yb_{1.94}Cr_{0.06}W_3O_{12}$ at high temperatures, which shortens the distance between the sensitizer and activator ions, thereby enhancing energy transfer and improving the emission intensity. Additionally, the lattice contraction helps to increase the structural rigidity of the matrix, further enhancing the thermal stability of the phosphor. Upon exceeding 398 K, the fluorescence intensity begins to decline. In this temperature regime, the energy loss caused by thermally activated non-radiative processes outweighs the energy gain from enhanced energy transfer, resulting in an overall reduction of luminescence intensity.[43] Furthermore, batch-to-batch consistency tests were performed and the quantitative reproducibility metrics for PL intensity and temperature-dependent luminescence are shown in Figure S8 and S9. The normalized decay curves of the 1048 nm emission of the $Yb_{1.94}Cr_{0.06}W_3O_{12}$ phosphor at various temperatures are presented in Figure 4d. The lifetime values have been calculated utilizing eqs. (3)-(4), and the fitting parameters

and goodness factor of fitting are listed in Table S7. It can be seen that the lifetime first increased and then followed a decreasing trend as temperature increases.

3.4 Applications in night vision and NIR pc-LED

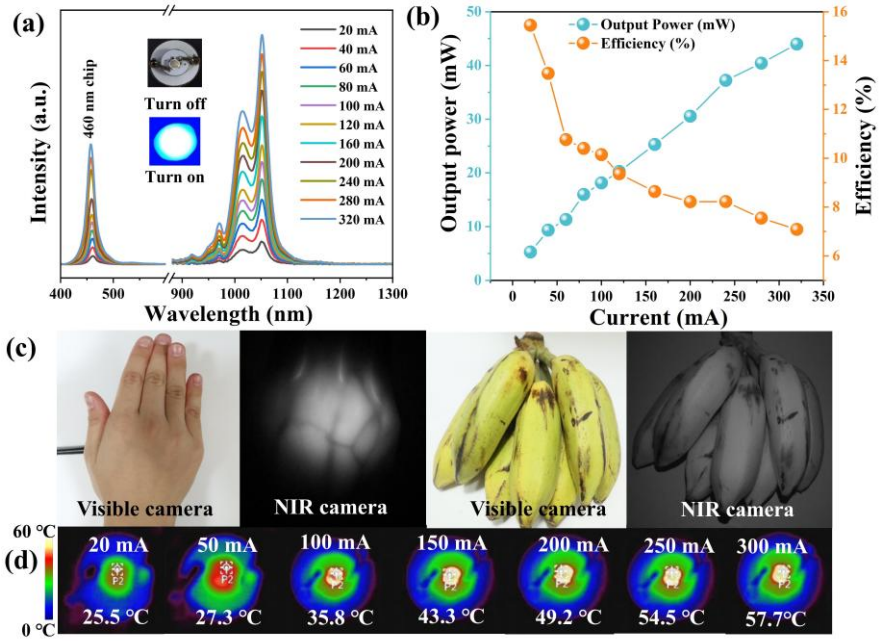


Figure 5. (a) Luminescence spectra obtained at different driving currents for the developed NIR pc-LED. (b) Relationships between photoelectric efficiency/NIR output power and the driving current. (c) Photographs demonstrating the practical application of the prepared NIR pc-LED device. (d) The thermographs obtained for the prepared device at varying driving current values (20-300 mA).

To evaluate the application potential of the obtained $Yb_{1.94}Cr_{0.06}W_3O_{12}$ phosphor, an NIR pc-LED device was fabricated by integrating this phosphor with a blue LED chip as the excitation source. The electroluminescence spectra of the prepared NIR pc-LED covered the NIR range extending from 900 to 1300 nm, as presented in Figure 5a. The FWHM of the spectra at different driving currents was calculated, and the spectral purity, an important parameter for applications such as biological imaging and composition identification, was obtained in Table S8. The small FWHM and high spectral purity may improve signal-to-noise ratio provide high accuracy in distinguishing different tissue absorption/scattering characteristics. The absolute NIR output power increases steadily at a higher driving current, reaching a value of 44 mW

and an irradiance of 1100 mA/cm^2 at 320 mA. The photoelectric efficiency for the prepared NIR pc-LED was found to be 15.4% at 20 mA (Figure 5b). Table S9 compares the performance of the $Yb_{1.94}Cr_{0.06}W_3O_{12}$ phosphor with those of previously reported Cr^{3+}-doped NIR phosphors. The outstanding photoelectric properties of our phosphor, combined with its anti-thermal quenching performance, demonstrate that the fabricated NIR pc-LED device holds great promise for practical applications. Taking into consideration the non-invasive and high penetration characteristics of NIR light, the prepared NIR pc-LED was employed as a light source for non-invasive imaging of human hand, and the results are shown in Figure 5c. Under the NIR light, the distribution of the endoskeleton in the finger was observed clearly. Meanwhile, a smartphone was used to take photos of fruits under natural light and were then passed through an NIR camera employing the fabricated NIR pc-LED as a light source, and the damage of the banana skin could be observed clearly with the NIR camera, which proved that our phosphor also has immense potential for night vision applications. As depicted in Figure 5d, the operating temperature of the fabricated device increased from 25.5 to 57.7 °C as the drive current increased from 20 to 300 mA, which is due to increased production of heat at higher current values. The temperature (T) and temperature rise (ΔT) as a function of the current are plotted in Figure S10.

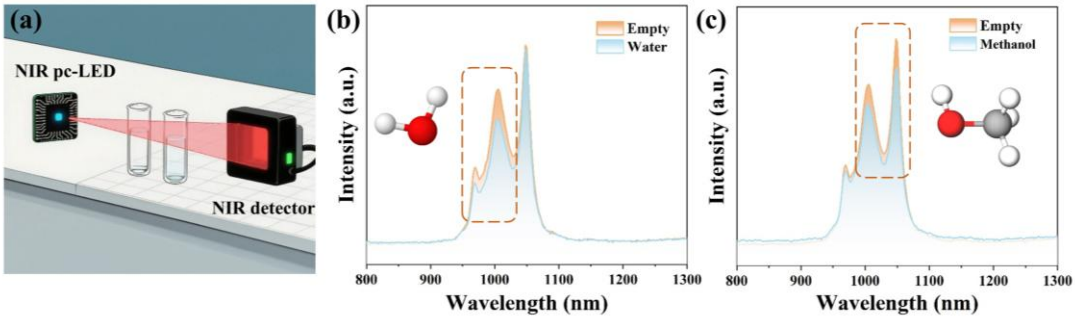


Figure 6. (a) Schematic diagram of the designed absorption spectroscopy testing system. The absorption spectra of (b) water and (c) methanol.

In order to highlight the potential application of the NIR-II pc-LED in the field of

NIR spectroscopy, a miniaturized real-time absorption spectroscopy testing system using this NIR pc-LED as the light source was designed, as shown in Figure 6a. The NIR-II region covers the vibrational frequencies of the functional groups such as C-H, O-H, and N-H in organic molecules. In this study, the NIR absorption spectra of water and methanol were measured. The results show that both the substances exhibit distinct absorption in the NIR region. Specifically, the spectrum of water in Figure 6b shows absorption bands at 970–1020 nm, which are attributed to the second overtone of O-H bond vibrations.[44,45] In Figure 6c, the absorption of methanol in the 900–1100 nm range is due to C-H bond vibrations.[46] The successful distinguishment of these two solutions highlights that the $Yb_{1.94}Cr_{0.06}W_3O_{12}$ phosphor may have good suitability for various portable NIR detection instruments. Inspired by previous research,[47–49] the application of the NIR phosphor in LiDAR technology can be expected since the excellent anti-thermal feature can effectively withstand the significant heat generated during LiDAR system operation to maintain a stable performance. Additionally, integrating the phosphor into flexible substrates to reduce hygroscopicity, which negatively impacts NTE properties, may allow wider applications of the phosphor.

4. CONCLUSIONS

$Yb_{2-2x}Cr_{2x}W_3O_{12}$ phosphor has been proposed in this study as a potential NIR light source material for developing NIR pc-LEDs. The results showed that trihydrate $Yb_2W_3O_{12}\cdot 3H_2O$ exhibits positive thermal expansion at room temperature. This behavior is attributable to the water molecules, which restrict the transverse thermal vibrations of Yb-O-W bonds. Upon heating to 373 K, dehydration occurs and the resulting orthorhombic $Yb_2W_3O_{12}$ demonstrates negative thermal expansion. The characteristic emission of Yb^{3+} within the range of 800-1300 nm was observed under 468 nm blue light irradiation due to efficient $Cr^{3+}\rightarrow Yb^{3+}$energy transfer. Notably, the

luminescence intensity of the $Yb_{1.94}Cr_{0.06}W_3O_{12}$ sample at 398 K is 1.89 times higher than that at room temperature. Such an anti-thermal quenching performance is superior over most long-wavelength-emitting NIR phosphors. This significant luminescence enhancement can be attributed to enhanced energy transfer from Cr^{3+} to Yb^{3+} by negative thermal expansion. This study thus provides a new strategy for developing NIR phosphors with anti-thermal quenching properties. Furthermore, the NIR pc-LED fabricated by combining the $Yb_{1.94}Cr_{0.06}W_3O_{12}$ phosphor with a blue LED chip exhibited an outstanding optoelectronic performance for potential application in night vision, non-invasive imaging, and compositional analysis.

ASSOCIATEDCONTENT

Supporting Information

ICP-MS results; EPR spectra; FE-SEM images; PLE/PL spectra of the matrix; decay curve and the decay fitting results; FWHM data and spectral purity; Rietveld refinement of XRD; The batch-to-batch consistency of PL intensity and thermal stability; A summary of performance parameter comparison (PDF)

AUTHOR INFORMATION

Corresponding Authors

Xuejiao Wang − *School of Materials and Environmental Engineering, Bohai University, Jinzhou, Liaoning 121007, P. R. China;* orcid.org/0000-0003-4327-2340; Email: wangxuejiao@bhu.edu.cn

Ji-Guang Li − *Research Center for Electronic and Optical Materials, National Institute for Materials Science, Tsukuba, Ibaraki 305-0044, Japan;* orcid.org/0000-0002-5625-7361; Email: li.jiguang@nims.go.jp

Authors

Sihan Yang − *School of Materials and Environmental Engineering, Bohai University, Jinzhou, Liaoning 121007, P. R. China*

Changshuai Gong − *School of Materials and Environmental Engineering, Bohai University, Jinzhou, Liaoning 121007, P. R. China*

Ziying Wang − *School of Materials and Environmental Engineering, Bohai University, Jinzhou, Liaoning 121007, P. R. China*

Liang Dong − *Key Laboratory for Anisotropy and Texture of Materials (Ministry of Education), School of Materials Science and Engineering, Northeastern University, Shenyang, Liaoning 110819, P. R. China*

Notes

The authors declare no competing financial interest. The authors also confirm that there are no undisclosed conflicts of interest related to citations of references.

ACKNOWLEDGEMENTS

This study was endorsed by the Liaoning Revitalization Talents Program (Grant No. XLYC2403017), the Natural Science Foundation of the Education Department of Liaoning Province (Grant No. JYTMS20231627), the Young Talents Program of Jinzhou (Grant No. JXYC230103), and the Innovation Fund Project for Graduate Student of Bohai University (Grant No. YJC2024-003). The authors would also like to acknowledge the support from Scientific Compass (www.shiyanjia.com).

REFERENCES

[1] Beć, K. B.; Grabska, J.; Huck, C. W. Near-infrared spectroscopy in bio-applications. *Molecules* **2020**, *25*(12), 2948.

[2] Vatansever, F.; Hamblin M. R. Far infrared radiation (FIR): Its biological effects and medical applications: Ferne Infrarotstrahlung: Biologische effekte und

medizinische anwendungen. *Photonics Lasers Med.* **2012**, *1*(4), 255-266.

[3] Hayashi, D.; van Dongen, A. M.; Boerekamp, J.; Spoor, S.; Lucassen, G.; Schleipen, J. A broadband LED source in visible to short-wave-infrared wavelengths for spectral tumor diagnostics. *Appl. Phys. Lett.* **2017**, *110*(23), 233701.

[4] Nicolaï, B. M.; Beullens, K.; Bobelyn, E.; Peirs, A.; Saeys, W.; Theron, K. I.; Lammertyn, J. Nondestructive measurement of fruit and vegetable quality by means of NIR spectroscopy: A review. *Postharvest Bio. Technol.* **2007**, *46*(2), 99-118.

[5] Chien, Y. H.; Chou, Y.; Wang. S.; Huang S.; Liau, M. C.; Chao, Y.; Su, C.; Yeh, C. S. Near-infrared light photocontrolled targeting, bioimaging, and chemotherapy with caged upconversion nanoparticles in vitro and in vivo. *Acs Nano* **2013**, *7*(10), 8516-8528.

[6] Rajendran, V.; Chang, H.; Liu, R. Recent progress on broadband near-infrared phosphors-converted light emitting diodes for future miniature spectrometers. *Opt. Mater. X* **2019**, *1*, 100011.

[7] Liu, D.; Dang, P.; Zhang, G.; Lian, H.; Li, G.; Lin, J. Near-infrared emitting metal halide materials: Luminescence design and applications. *Infomat* **2024**, *6*(5), No. e12542.

[8] Huang, W.; Chen, K.; Huang, M.; Liu, R. Tunable spinel structure phosphors: Dynamic change in near-infrared windows and their applications. *Adv. Opt. Mater.* **2023**, *11*(23), 2301166.

[9] Payne, S. A.; Chase, L. L.; Smith, L. K.; Kway, W. L.; Newkirk, H. W. Laser performance of $LiSrAlF_6$: Cr^{3+}. *J. Appl. Phys.* **1989**, *66*(3), 1051-1056.

[10] Sun, A.; Guo, H.; Gan, Q.; Yang, L.; Liu, Q.; Xi, L. Evaluation of visible NIR-I and NIR-II light penetration for photoacoustic imaging in rat organs. *Opt. Express.* **2020**, *28*(6), 9002-9013.

[11] Xu, X.; Han, P.; Zheng, D.; Du, K.; Li, C.; Liu, F.; Zhang, R.; Han, K. Boosting the upconversion and near-infrared emission *via* alloying Bi^{3+} in $Cs_2NaErCl_6$ double perovskite. *Laser Photonics Rev.* **2022**, *16*(11), 2200318.

[12] Peralta, X. G.; Clary, J. E.; Peterson, A. M.; Noojin, G. D.; Lund, B. J.; Echeverria, F. J.; Rockwell, B. A. Evaluation of the potential eye hazard at visible wavelengths of the supercontinuum generated by an ultrafast NIR laser in water. *Biomed. Opt. Express* **2021**, *12*(2), 1167-1180.

[13] Wang, Y.; Chen, B.; Wang, F. Overcoming thermal quenching in upconversion nanoparticles. *Nanoscale* **2021**, *13*(36), 3454-3462.

[14] Zou, H.; Yang, X.; Chen, B.; Du, Y.; Ren, B.; Sun, X.; Qiao, X.; Zhang, Q.; Wang, F. Thermal enhancement of upconversion by negative lattice expansion in orthorhombic $Yb_2W_3O_{12}$. *Angew. Chem. Int. Ed.* **2019**, *58*(48), 17255-17259.

[15] Sumithra, S.; Umarji, A. M. Role of crystal structure on the thermal expansion of $Ln_2W_3O_{12}$ (Ln = La, Nd, Dy, Y, Er and Yb). *Solid State Sci.* **2004**, *6*(12), 1313-1319.

[16] Furuse, H.; Yasuhara, R.; Hiraga, K. Thermo-optic properties of ceramic YAG at high temperatures. Opt. Mater. Express **2014**, *4*(9), 1794-1799.

[17] Qiao, Y.; Sun, D.; Zhang, H.; Luo, J.; Quan, C.; Dong, K.; Chen, Y.; Wang, Z.; Li, H.; Cheng, M. Thermal, spectroscopy and optimized ~3 μm CW laser properties for Ho, Pr: YAP crystal. Opt. Express **2023**, *31*(22), 36429-36438.

[18] Chen, Z.; Cun, Y.; Yan, S.; Zi, Y.; Zhu, B.; Ruan, K.; Ding, B.; Yang, Z.; Haider, A. A.; Khan, I.; Tatiana, C.; Qiu, J.; Huang, A.; Liu, Y.; Yang, Z. Negative and positive thermal expansion effects regulate the upconversion and near-infrared downshift luminescence for multiparametric temperature sensing. *Sci. China Mater.* **2023**, *66*(12), 4742-4748.

[19] China Jiliang University. A Fluorescent Thermal Enhancement Ceramic Glass and Its Preparation Method and Application. CN118908571A, Nov 8, 2024.

[20] Jin, X.; Sun, P.; Yang, W.; Wang, Y.; Xiao, Z. Thermal enhancement of upconversion luminescence in negative-thermal-expansion Ho^{3+}-doped $Yb_{2-x}W_3O_{12}$ phosphors. *J. Electron. Mater.* **2024**, *53*(9), 4929-4938.

[21] Shannon, R. D. Revised effective ionic radii and systematic studies of interatomic distances in halides and chalcogenides. *Acta crystallogr. A*. **1976**, *32*(5),751-767.

[22] Yang, S.; Xue, X.; Jiang, F.; Dong, L.; Zhu, Q.; Wang, X.; Li, J.-G. A novel $KSrScSi_2O_7$: *x*Cr silicate phosphor, luminescence/chromaticity, and applications in NIR pc-LED and stable green ceramic pigments. *J. Rare Earths* **2024**.

[23] Yue, Y.; Wang, T.; Yan, Y.; Guo, L.; Zhu, X.; Bu, W.; Wang, G.; Zhu, N.; Zhao, L.; Yu, X. Nonstoichiometry-induced self-activated phosphors for dynamic anti-counterfeiting applications. *ACS Appl. Mater. Interfaces* **2024**, *16*(25), 32402-32410.

[24] Niu, Y.; Wu, F.; Zhuo, Y.; Li, J.; Zhang, Q.; Teng, Y.; Xie, X.; Dong, H.; Mu, Z. Luminescence properties and applications of Ca_2ScTaO_6: Bi^{3+}, Ln^{3+} (Ln = Eu, Sm, Dy, Tb) phosphors. *Ceram. Int.* **2025**, *51*(20), 30597-30603.

[25] Zhuo, Y.; Niu, Y.; Wu, F.; Li, J.; Wang, Y.; Zhang, Q.; Teng, Y.; Xie, X.; Dong, H.; Mu, Z. Super-wide-range tunable emission across NIR-II and NIR-III achieved by B-site cation co-substitution in Ni^{2+}-doped double perovskites for NIR light sources. *J. Mater. Chem. C* **2025**, *21*, 10621-10631.

[26] Wang, X.; Yang, S.; Jiang, F.; Wang, J.; Gong, C.; Li, J.-G. Broadband photoluminescence toward the NIR II region and stable green ceramic pigments based on a novel $NaBaScSi_2O_7$: *x*Cr silicate phosphor. *J. Mater. Chem. C* **2025**, *13*(12), 6364-6374.

[27] Wang, Z.; Lei, R.; Wang, H.; Li, D.; Xu, S. Anti-thermal quenching luminescence and water resistance in Nd^{3+}-doped $Yb_2M_3O_{12}$ (M = Mo, W) phosphors and phosphor-in-glass composites. *J. Alloys Compd.* **2025**, *1010*, 178202.

[28] Li, Q.; Yuan, B.; Song, W.; Liang, E.; Yuan, B. The phase transition, hygroscopicity, and thermal expansion properties of $Yb_{2-x}Al_xMo_3O_{12}$. Chin. Phys. B **2012**, *21*(4), 046501.

[29] Zhang, Y.; Jin, M.; Chen, W.; Wu, Z.; Li, Z.; Guo. C. Thermally enhanced NIR up-conversion fluorescence multimode thermometry based on $Y_2Mo_3O_{12}$: Nd^{3+}, Yb^{3+}. *J. Mater. Chem. C* **2024**, *12*, 7588-7595.

[30] Zhang, L.; Xia, Y.; Shen, X.; Yang, R.; Wei, W. Investigations on the effects of the Stark splitting on the fluorescence behaviors in Yb^{3+}-doped silicate, tellurite, germanate, and phosphate glasses. *Opt. Mater.* **2018**, *75*, 1-6.

[31] Wei, S.; Lyu, Z.; Sun, D.; Shen, S.; Zhang, X.; Lu, Z.; Luo, P.; Hu, H.; You, H. A NIR phosphor with ultra-broadband emission enabled by dual energy transfer within two Cr^{3+} emitters and $Cr^{3+}\rightarrow Yb^{3+}$. *J. Mater. Chem. C* **2024**, *12*, 4977-4985.

[32] Zheng, S.; Ma, S.; He, S.; Guan, Q.; Chao, L.; Qiao, J.; Ma, Y. Luminescence

properties and energy transfer of broadband NIR phosphor Li_2MgZrO_4: 1.0%Cr^{3+}, *y*%Yb^{3+}. *Spectrochim. Acta Part A* **2024**, *314*, 124200.

[33] Li, J.; Wang, C.; Niu, Y.; Wang, Y.; Wu, F.; Zhang, Q.; Teng, Y.; Dong, H.; Mu, Z. Efficient broad-band NIR-II emitting phosphor $Mg_4Ta_2O_9$: Ni^{2+} with satisfactory thermal stability of luminescence. *Ceram. Int.* **2024**, *50*(11), 18647-18654.

[34] Zhang, Q.; Liu, D.; Dang, P.; Lian, H.; Li, G.; Lin, J. Two selective sites control of Cr^{3+}-doped ABO_4 phosphors for tuning ultra-broadband near-infrared photoluminescence and multi-applications. *Laser Photonics Rev.* **2022**, *16*(2), 2100459.

[35] Xiao, Q.; Zhou, W.; Fan, J.; Zhou, L.; Chen, P.; Mo, F.; Huang, J.; Liu, X.; Zhang, X. Synthesis and luminescent properties of $ZnWO_4$: Cr^{3+} nanoparticles for NIR-II fluorescence imaging. *Ceram. Int*. **2023**, *49*(15), 25682-25688.

[36] Zhang, A.; Liu, Y.; Liu, G.; Xia, Z. Dopant and Compositional Modulation Triggered Broadband and Tunable Near-Infrared Emission in $Cs_2Ag_{1-x}Na_xInCl_6$: Cr^{3+} Nanocrystals. *Chem. Mater.* **2022**, *34*(7):3006-3012.

[37] Liu, G.; Molokeev, M. S.; Xia, Z. Structural rigidity control toward Cr^{3+}-based broadband near-infrared luminescence with enhanced thermal stability. *Chem. Mater.* **2022**, *34*(3), 1376-1384.

[38] Machado, T. M.; Costa, I. L. M.; Dosen, A.; de Faro Melo, G. S. L.; Vasconcellos, L. E.; Marinkovic, B. A. Hygroscopicity, phase transition and thermal expansion in $Yb_{2-x}Ga_xW_3O_{12}$ system. *J. Alloys Compd.* **2021**, *854*: 156643.

[39] Kol'Tsova, T. N. X-ray Diffraction Study of $Y_2W_3O_{12}\cdot 3H_2O$. *Inorg. Mater.* **2001**, *37*(11), 1175-1177.

[40] Yu, Z.; Peng, J.; Wang, H.; Wu, M.; Cheng, Y.; Hu, Z.; Chen, D. Thermal expansion properties and hygroscopicity of $Y_{2-x}Sm_xW_3O_{12}$ (x = 0.0-0.4) compounds. *Sci. China Ser. E* **2008**, *51*(1), 25-32.

[41] Fu, B.; Yan, H.; Li, R.; Liao, Z.; Qiu, Bao.; Gong, G.; Huang, H.; Sun, Y.; Wen, H. -R.; Liao, J. Simultaneously tuning the luminescent color and realizing an optical temperature sensor by negative thermal expansion in $Sc_2(WO4)_3$: Tb/Eu phosphors. *Dalton Trans.* **2024**, *53*(2), 798-807.

[42] Marinkovic, B. A.; Pontón, P. I.; Romao, C. P.; Moreira, T.; White, M. A. Negative and near-zero thermal expansion in $A_2M_3O_{12}$ and related ceramic families: a review. *Front. Mater.* **2021**, *8*, 741560.

[43] Wang, Z.; Lei, R.; Zhao, S.; Huang, F.; Xu, S. Design and analysis of PiG-based ratiometric thermometer integrating positive and negative thermal quenching materials. *Opt. Mater.* **2025**, *160*, 116787.

[44] Yang, S.; Li, X.; Zhang, Q.; Li, M.; Wang, X.; Wu, N. Efficient energy transfer in $NaBaScSi_2O_7$: Cr^{3+}, Er^{3+} phosphor enabling simultaneously strong NIR-II/III emissions for diversified applications. *Opt. Mater.* **2025**, *168*, 117385.

[45] Liu, J.; Sun, D.; Lyu, Z.; Shen, S.; Wei, S.; Zhou, L.; Zhang, X.; Hu, H.; You, H. Tunable luminescence in $LiSc_{1-y}Ga_yW_2O_8$: Cr^{3+} phosphors for LED applications. *Adv. Opt. Mater.* **2024**, *12*(35), 2401883

[46] Li, Z.; Zhu, G.; Li, H.; Zhu, Q.; Cong, Y.; Bai, X.; Li, J.; Dong, B. Visible light excited Yb^{3+}-doped phosphor *via* Eu^{2+} bridged energy transfer toward NIR-II spectroscopy application. *Laser Photonics Rev.* **2025**, *19*(14), 2402162.

[47] Xue, T.; Liang, W.; Li, Y.; Sun, Y.; Xiang, Y.; Zhang, Y.; Dai, Z.; Duo, Y.; Wu, L.; Qi, K.; Shivananju, B.; Zhang, L.; Cui, X.; Zhang, H.; Bao, Q. Ultrasensitive

detection of miRNA with an antimonene-based surface plasmon resonance sensor. *Nat. commun.* **2019**, *10*(1), 28.

[48] Guo, Z.; Cao, R.; Wang, H.; Zhang, X.; Meng, F.; Chen, X.; Gao, S.; Sang, D. K.; Nguyen, T. H.; Duong, A. T.; Zhao, J.; Zeng, Y. -J.; Cho, S.; Zhao, B.; Tan P.-H.; Zhang, H.; Fan, D. High-performance polarization-sensitive photodetectors on two-dimensional β-InSe. *Natl. Sci. Rev.* **2022**, *9*(5), nwab098.

[49] Xu, Y.; Shi, X.; Zhang, Y.; Zhang, H.; Zhang, Q.; Huang, Z.; Xu, X.; Guo, J.; Zhang, H.; Sun, L.; Zeng, Z.; Pan, A.; Zhang, K. Epitaxial nucleation and lateral growth of high-crystalline black phosphorus films on silicon. *Nat. commun.* **2020**, *11*(1), 1330.

Graphical Abstract

